Earth and Planetary Science Letters 335–336 (2012) 195–205

Contents lists available at SciVerse ScienceDirect

Earth and Planetary Science Letters

journal homepage: www.elsevier.com/locate/epsl

Uppermost mantle structure of the eastern margin of the Tibetan plateau from interstation *Pn* traveltime difference tomography

Zhiwei Li [a], Sidao Ni [a,*], Tianyao Hao [b], Yi Xu [b], Steven Roecker [c]

[a] State Key Laboratory of Geodesy and Earth's Dynamics, Institute of Geodesy and Geophysics, Chinese Academy of Sciences, Wuhan 430077, China
[b] Key Laboratory of Petroleum Resource Research, Institute of Geology and Geophysics, Chinese Academy of Sciences, Beijing 100029, China
[c] Department of Earth and Environmental Sciences, Rensselaer Polytechnic Institute, Troy, NY 12180, USA

ARTICLE INFO

Article history:
Received 10 January 2012
Received in revised form
3 May 2012
Accepted 6 May 2012
Editor: P. Shearer

Keywords:
eastern Tibetan plateau
Wenchuan earthquake
traveltime tomography
uppermost mantle
Pn traveltime difference
Longmenshan Fault Belt

ABSTRACT

Tomographic inversion with interstation *Pn* differential traveltime data provides a reliable velocity image of the uppermost mantle across the Longmenshan Fault Belt, which borders the eastern Tibetan plateau and Sichuan Basin. Low *Pn* velocities (<7.8 km/s) are revealed beneath the eastern Tibetan plateau to the west of the Longmenshan Fault Belt, while high *Pn* velocities (>8.1 km/s) appear beneath the Sichuan Basin to the east, suggesting a relatively weak upper mantle beneath eastern Tibetan plateau and a strong upper mantle beneath the Sichuan Basin. The *Pn* velocities are consistent with the proposition that the rigid and stable lithosphere of the Sichuan Basin may act as a barrier to the eastward escape flow of the ductile crust of the eastern Tibetan plateau. Consistency of *Pn* velocities with the smoothed topography, crustal thickness and Bouguer gravity implies that the dynamic processes of the lithospheric mantle should be responsible for the crustal thickening and relief of uplift in the eastern Tibetan plateau. However, the Longmeshan Fault Belt appears to be separated into two segments by the Huya and Leidong faults as manifested by significant discrepancies in topography gradient, seismic activity, rupture process and aftershock distribution of Wenchuan earthquake. This segmentation is also supported by difference in *Pn* velocities along the strike of the fault belt, suggesting different tectonic environments in the crust and lithospheric mantle. Understanding of the mechanism for the segmentation requires further investigation.

1. Introduction

As one of the most impressive tectonic features on the Earth, the high elevations (greater than 4000 m) and thickened crust (60–70 km) of the Tibetan plateau are believed to be the result of ~2000 km shortening during the Indian–Eurasian continental collision over the last 50 million years (Molnar and Tapponnier, 1975; Molnar, 1988). The margins of Tibetan plateau typically show steep slopes and active seismicity, but the eastern margin is particularly unusual. First, the east margin features the steepest topography gradient in the world (Burchfiel et al., 2008) (Fig. 1). The eastern margin is located between the Tibetan plateau and the Yangtze craton, and rises steeply westward from ~500 m in the Sichuan Basin to >4000 m elevation in the eastern Tibetan plateau within~50 km horizontal distance. Moreover, the crust thickens rapidly from ~40 km in the Sichuan Basin to >60 km in the eastern Tibetan plateau (Wang et al., 2003, 2008a; Xu et al., 2007; Burchfiel et al., 2008; Yao et al., 2008; Zhang et al., 2009). Second, the east margin is the location of devastating earthquakes within a region of slow deformation (Zhang et al., 2004, 2008). In this region, the Longmenshan Fault Belt (LFB) forms the tectonic boundary between the eastern Tibetan plateau and the Sichuan Basin. On 12 May 2008, the Wenchuan M_w 7.9 earthquake occurred in the southwestern portion of the LFB and ruptured over a length of ~300 km along the LFB (Burchfiel et al., 2008; Ji and Hayes, 2008; Wang et al., 2008b; Zhang et al., 2008). As the most devastating earthquake since the Tangshan M_L 7.8 earthquake on 28 July 1976 in China, the Wenchuan earthquake intrigued geoscientists due to its huge magnitude for a slowly deforming fault system. Very few strong seismic events (only 3 earthquakes with magnitude of 6–6.5 occurred since the year of 1657) have ever occurred along the LFB (Wen, 1995). Modern geodetic surveys show a slow slip rate (<3 mm/yr) across the LFB (Zhang et al., 2008). In addition, Global Positioning System (GPS) observations suggest that relatively minor shortening (<2 mm/yr) is present across the entire LFB less than 1 mm/yr shortening across various individual fault strands (Zhang et al., 2004, 2008).

Although the Wenchuan earthquake ruptured over a length of ~300 km along the LFB as inferred from finite fault waveform

* Corresponding author.
E-mail address: sdni@whigg.ac.cn (S. Ni).

0012-821X/$ - see front matter © 2012 Elsevier B.V. All rights reserved.
http://dx.doi.org/10.1016/j.epsl.2012.05.005

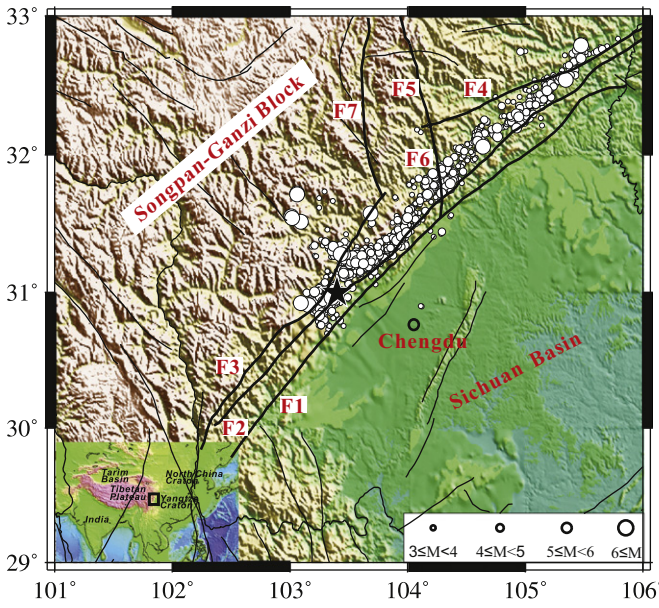

Fig. 1. Wenchuan main shock (star), aftershocks (open circle) and faults (black traces) overlaid on a topographic map of the eastern Tibetan Plateau, west Sichuan Basin, and surrounding regions. The Longmenshan Fault Belt (LFB) mainly consists of three major faults from the east to the west: Guanxian-Jiangyou Fault, Yingxiu-Beichuan Fault, and Wenchuan-Maoxian Fault, which are indicated by F1, F2, and F3, respectively. Other faults, F4 Pingwu-Qingchuan Fault; F5 Huya Fault; F6 Leidong Fault; F7 Minjiang Fault.

inversion and spatial pattern of aftershocks, the southwestern and northeastern portions of the LFB (roughly beginning at ~N31.5°) still have significant differences in seismic activity and rupture process (Wen, 1995; Zhang et al., 2008; Huang et al., 2008; Chen et al., 2009; Zheng et al., 2009). The only three strong earthquakes (with magnitude of 6.0–6.5) before the occurrence of the Wenchuan earthquake since the year of 1657 all occurred in the southwestern portion of the LFB, while no strong earthquake was recorded in the northeastern portion (Wen, 1995; Chen et al., 2007). The northern segment of LFB was even claimed to be seismically inactive because of the lack of historical seismicity and other tectonic features (Chen et al., 2007). GPS observation is also consistent with low historical seismic activity in the northeastern portion of the LFB (Zhang et al., 2008). Moreover, in the southwestern portion of the LFB, the Wenchuan earthquake ruptured along several faults (i.e., the Wenchuan-Maoxian fault, Yingxiu-Beichuan fault and Guanxian-Jiangyou fault) to the surface (Fig. 1), while only one fault (i.e., the Yingxiu-Beichuan fault) ruptured in the northeastern portion. A thrust mechanism with a small dip angle of 30–50° dominates the rupture in the southwestern portion of the LFB, but thrust and dextral right-slip mechanism control the rupture in its northeastern portion with a larger dip angle of 70–90° (Wang et al., 2008b; Xu et al., 2008; Zheng et al., 2009; Luo et al., 2010). Whether the different characteristics of the faults and co-seismic ruptures in the southwestern and northeastern portions are related to the deep dynamics of the upper mantle or not needs to be investigated.

Seismic imaging has become one of the most effective methods to reveal possible links between subsurface velocity structure and seismic activities. Recent seismological studies, such as 3-D travel time tomography (e.g., Wang et al., 2003; Guo et al., 2009; Wu et al., 2009; Lei and Zhao, 2009; Xu et al., 2010a; Xu and Song, 2010; Li et al., 2011a), surface wave tomography with seismic ambient noise (e.g., Yao et al., 2008; Li et al., 2009a, 2010; Yang et al., 2010; Zheng et al., 2010), deep sounding profiles (e.g., Wang et al., 2003), as well as receiver function imaging (e.g., Wang et al., 2008a; Liu et al., 2009; Zhang et al., 2009, 2010) clearly show significant variations of seismic velocity in the crust and mantle across LFB. Those results suggest that the eastward movement of the Tibetan Plateau with a weak mid-lower crust is blocked by the strong lithosphere of the Sichuan Basin as suggested by higher velocity in the deep crust and upper mantle (Clark and Royden, 2000). This model provides one possible explanation for the rapid uplift and crustal thickening of the Tibetan plateau, as well as the small relative horizontal movement (<2 mm/yr) across the entire LFB from GPS observations (Zhang et al., 2004; Burchfiel et al., 2008; Zhang et al., 2008; Zhang et al., 2010).

Accurate imaging of the uppermost mantle would also provide additional key information about the ongoing continental collision and its probable contribution to occurrence of the Wenchuan earthquake. However, in the eastern Tibetan plateau, the high resolution velocity structure of the uppermost mantle has not been well investigated except for some relatively low resolution *Pn* tomographic results (Zhao and Xie, 1993; McNamara et al., 1997; Hearn et al., 2004; Liang et al., 2004; Phillips et al., 2005; Liang and Song, 2006; Pei et al., 2007; Cui and Pei, 2009; Xu and Song, 2010; Xu et al., 2010b). On one hand, most of previous *Pn* tomographic studies in this area are not focused on the LFB and its relations to the Wenchuan earthquake. On the other hand, relatively large errors of earthquake location and origin time in this area could greatly compromise standard *Pn* tomographic inversions with absolute *Pn* arrival times. The analysis of earthquake location robustness in the Sichuan province by Sun et al. (2004) suggests that the differences of both the epicenter and the focal depth after relocation can be as large as 10 km, as compared to the earthquake catalogs from the Sichuan Earthquake Network. Therefore, it is helpful to adopt a more robust and reliable method to conduct the *Pn* tomographic inversion in this area.

The travel time difference between seismic arrivals can greatly improve the reliability of both earthquake location and velocity structure (Waldhauser and Ellsworth, 2000; Zhang and Thurber, 2003). Recent studies suggest that the usage of interstation *Pn* traveltime difference data from one seismic event to a pair of stations can substantially reduce tomography errors due to source terms (e.g., the errors of earthquake origin time and location, especially the focal depth) when certain geometric requirements are met (Phillips et al., 2005; Seward et al., 2009). Phillips et al. (2005) and Seward et al. (2009) utilized the interstation *Pn* traveltime difference data to conduct *Pn* tomography in China and New Zealand, respectively, and achieved more reliable and robust velocity images of the uppermost mantle. The *Pn* velocities beneath the North China craton has also been achieved by this method (Li et al., 2011b). Their results prove that the *Pn* traveltime difference techniques reliably improve *Pn* velocity images. In this study, we attempt to obtain a reliable and high resolution velocity image of the uppermost mantle across the LFB via tomographic inversion with interstation *Pn* traveltime difference data. With the uppermost mantle velocity structure resolved, we discuss the tectonic implications between the eastern Tibetan and the Sichuan Basin, and explore the potential relations between the deep dynamics of the mantle lid and the various aspects of the Wenchuan earthquake along the LFB.

2. Method and data

2.1. Interstation Pn traveltime difference tomography

Pn traveltime tomography has become an important tool to image the velocity structure in the uppermost mantle (Hearn, 1996; Hearn et al., 2004). In the standard approach of *Pn* traveltime tomography, absolute *Pn* traveltime data is used to conduct the inversion, and event and station terms are used

to accommodate the lateral variations of crustal structure, as well as the errors of earthquake location and origin time (Hearn, 1996; Hearn et al., 2004; Liang et al., 2004; Pei et al., 2007; Liang and Song, 2006). Since the absolute *Pn* travel time is easily contaminated by the errors of earthquake source parameters which then compromise the tomographic result, it is beneficial to find a robust method to minimize these uncertainties in achieving a reliable *Pn* tomographic image. Such a method is particularly necessary for studies in the eastern margin of the Tibetan plateau with relatively sparse stations and strongly heterogeneous crustal structure.

The traveltime differences of seismic arrivals often provide better constraints in earthquake relocation (Waldhauser and Ellsworth, 2000) and traveltime tomography (Zhang and Thurber, 2003). For *Pn* arrivals, when an earthquake lies approximately on the extension of the great circle path connecting two stations, the portion of *Pn* wave travel times along the overlapped ray paths are almost identical (Fig. 2) (Phillips et al., 2005; Seward et al., 2009; Li et al., 2011b). To demonstrate this, we simulate the variation of *P* (including *Pn*) wave traveltime differences between a pair of stations followed the method proposed by Phillips et al. (2005). The sources were set at each grid point with a depth of 10 km and perturbed using 200 realizations of 10 km Gaussian random noise in three dimensions. If the focal depth becomes less than zero, it was set to zero (Phillips et al., 2005). The standard deviations of the time differences are plotted on a logarithmic scale in Fig. 3. The result shows the variations of *Pn* traveltime differences are less than ~0.1 s when the events lie approximately on the great circle path connecting the two stations (Li et al., 2011b). It suggests that the *Pn* traveltime differences are insensitive to the mislocation of earthquake. The origin time error is also completely eliminated because the time difference is used. Moreover, the effects of lateral crustal structure near the source region can also be minimized because *Pn* waves for the two stations share almost identical ray paths in the source-side crust (i.e., near the earthquake). Recent studies also demonstrate that the *Pn* traveltime difference technique leads to more reliable and robust estimates of the velocity structure of the uppermost mantle (Phillips et al., 2005; Seward et al., 2009; Li et al., 2011b). The effects due to Moho topography can also be introduced into the inversion to correct for the station delay and improve the tomographic image (Li et al., 2011b).

In this study, we follow the basic inversion scheme for the *Pn* wave by Hearn (1996), and assume *Pn* wave propagates along great circle path. But we only consider the isotropic case because there are not enough *Pn* ray paths to solve for anisotropic parameters in the study region. Assuming an isotropic velocity model in the uppermost mantle, *Pn* traveltime residuals can be described by the following equation (Hearn, 1996; Hearn et al., 2004):

$$t^r = t^o - t^c = \Delta t^{st} + \Delta t^{eq} + \sum_{k=1}^{N} d_k s_k \quad (1)$$

where t^r is the *Pn* traveltime residual; t^o and t^c are the observed and calculated *Pn* traveltimes from the earthquake to the station; Δt^{st} is the difference between observed and calculated traveltimes traveling from the Moho discontinuity to the station, which depends on crustal velocity and thickness; Δt^{eq} is the difference between observed and calculated traveltime from the *j*th event to the Moho discontinuity, which depends on focal depth and crustal structure; d_k is the ray path length in the *k*th cell, and s_k is the slowness perturbation of this cell.

For a specific earthquake, the interstation *Pn* traveltime difference between stations *i* and *j* can be represented as

$$\Delta t_{ij} = t_i - t_j = \left(\sum_{k=1}^{N_i} d_{ik}s_{ik} + \Delta t_i^{eq} + \Delta t_i^{sta}\right) - \left(\sum_{k=1}^{N_j} d_{jk}s_{jk} + \Delta t_j^{eq} + \Delta t_j^{sta}\right)$$

$$= \left(\sum_{k=1}^{N_i} d_{ik}s_{ik} - \sum_{k=1}^{N_j} d_{jk}s_{jk}\right) + (\Delta t_i^{eq} - \Delta t_j^{eq}) + (\Delta t_i^{sta} - \Delta t_j^{sta}) \quad (2)$$

where t_i and t_j are the *Pn* traveltimes at station *i* and *j*; Δt_{ij} is the interstation traveltime difference; d_{ik} and d_{jk} are the *k*th ray path lengths traveling through the uppermost mantle, N_i and N_j segments in total; S_{ik} and S_{jk} are the corresponding *Pn* wave slowness at the *k*th ray path segment; $\Delta t_i^{eq}$and $\Delta t_j^{eq}$are the traveltimes in the source-side crust; $\Delta t_i^{sta}$and $\Delta t_j^{sta}$are the traveltimes in the station-side crust. In Eq. (2), the origin time of the event in Δt_i^{eq} and Δt_j^{eq}has been eliminated, and only the effect of event mislocation (especially the error of focal depth) remains. Based on the analyses by Li et al. (2011b), Δt_i^{eq} and Δt_j^{eq}in Eq. (2) are almost the same when the earthquake lies approximately on the great circle path connecting the two stations. Hence, the interstation *Pn* traveltime difference can be expressed as

$$\Delta t_{ij} = t_i - t_j = (\Delta t_i^{sta} - \Delta t_j^{sta}) + \left(\sum_{k=1}^{N_i} d_{ik}s_{ik} - \sum_{k=1}^{N_j} d_{jk}s_{jk}\right) \quad (3)$$

where the effect of the earthquake source parameters has been eliminated and the event mislocation has no effect on the *Pn* traveltime difference. For the linear system of Eq. (3), given the reference model and proper grid spacing, we can solve the slowness perturbations (Δs_{lk}) of the uppermost mantle and the station delays (Δt_i^{sta}andΔt_j^{sta}) simultaneously. The damped LSQR algorithm (Paige and Saunders, 1982) is used to solve the linear system. Smoothness constraints are also imposed to emphasize the more coherent long-wavelength structures. The effect is to remove small-scale variations on the order of 1–2 grid lengths (Li et al., 2009b, 2011b).

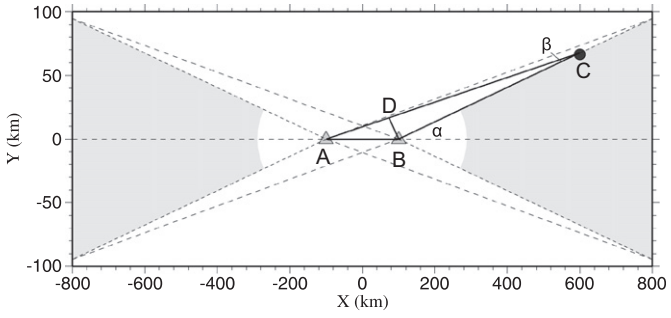

Fig. 2. Sketch of interstation traveltime differences from one earthquake (dot) to two stations (Gray triangles, A and B). Lines CA and CB represent the ray path from earthquake C to the stations A and B in the uppermost mantle, respectively. AB is the interstation distance. Gray shadows indicate the area where the earthquake is near the great circle path connecting two stations with a maximum angle α. β is the angle between the ray paths from the earthquake to the two stations, which is always less than α. *D* is the point at the ray path CA, which makes the length of CD equal to that of CB. Hence, BD represents the maximum distance between the ray paths CA and CB with the same epicenter distances to the earthquake. The ray path difference (AD) is used in the tomographic inversion.

2.2. Data

The data used in this study are seismic arrivals from the Sichuan Earthquake Network for earthquakes during the period of January 2000 to April 2008, i.e., about 8 years of data before the Wenchuan earthquake. A similar dataset was used by previous 3-D crustal traveltime tomographic inversions in this area (Lei and Zhao, 2009; Xu and Song, 2010; Wu et al., 2009; Li et al., 2011a). To control the quality of the data, three steps are taken to choose the *Pn* traveltime differences for this study. In the first step, we choose earthquakes with at least 5 arrivals and absolute residuals less than 3.5 s. In total, 103 stations, 7252

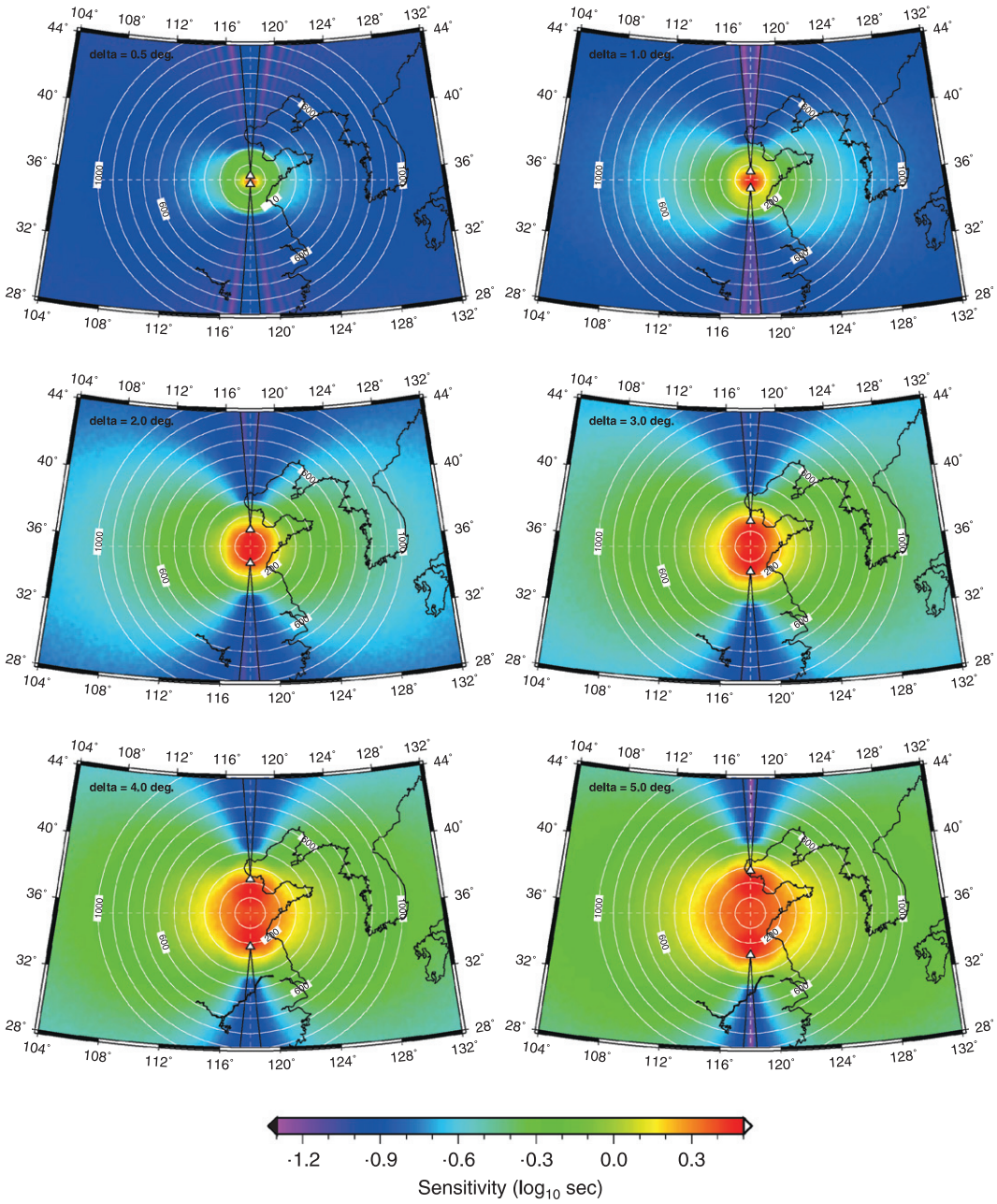

Fig. 3. Standard derivations of interstation first P arrival differences due to the earthquake mislocation with 200 random trials for different interstation distances. Concentric circles are plotted in increments of 100 km from the middle of two stations. The area between the solid black lines indicates the region within 6° azimuth of the straight line through two stations. In this area, variations of P wave traveltime differences are less than ~0.1 s.

earthquakes, and 68,814 *P* and *Pn* wave arrivals are available after this step. In the second step, *Pn* arrivals are extracted from this dataset with the following criteria: (1) the minimum epicenter distance is set to be 300 km to avoid misidentification of *P* as *Pn* arrivals; (2) each earthquake has at least 5 *Pn* arrivals. In the third step, interstation *Pn* traveltime differences are chosen from the culled *Pn* arrivals with following criteria: (1) the angle between the back azimuths from the event to the two stations (i.e., angle α in Fig. 2) is less than 6°, which ensures the two *Pn* ray paths are close enough; (2) the distance between two stations for each interstation *Pn* traveltime difference is greater than 50 km to ensure enough sampling of the uppermost mantle; (3) the traveltime difference residual is less than both 3.0 s and 10% of its total traveltime difference at the same time.

As a result of this procedure, a set of 328 *Pn* traveltime differences from 57 stations and 160 earthquakes are selected to conduct the *Pn* tomography. The events, stations and ray paths sampling the uppermost mantle are shown in Fig. 4. We note that the data coverage is reasonably good in the vicinity of the LFB.

2.3. Initial model

The average *Pn* velocity (~7.9 km/s) of the uppermost mantle was determined by linear fitting with interstation *Pn* traveltime difference data, and it is close to the average *Pn* velocity found by previous studies in this area (Cui and Pei, 2009; Xu et al., 2010b). Fig. 5a shows the interstation *Pn* wave traveltime difference versus epicenter distance difference (i.e., the inter station distance) from an earthquake recorded by two stations. The linear

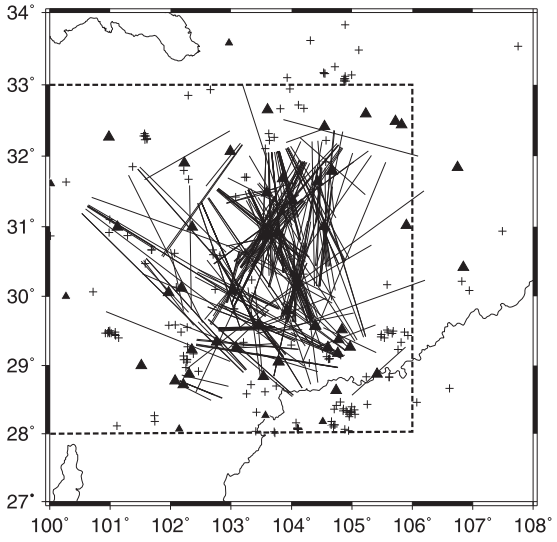

Fig. 4. *Pn* traveltime difference data from stations (triangles) and earthquakes (crosses) used in this study. Solid lines show the ray paths approximately sampling the uppermost mantle, which are used in the tomographic inversion. Dashed lines indicate the area with tomographic results.

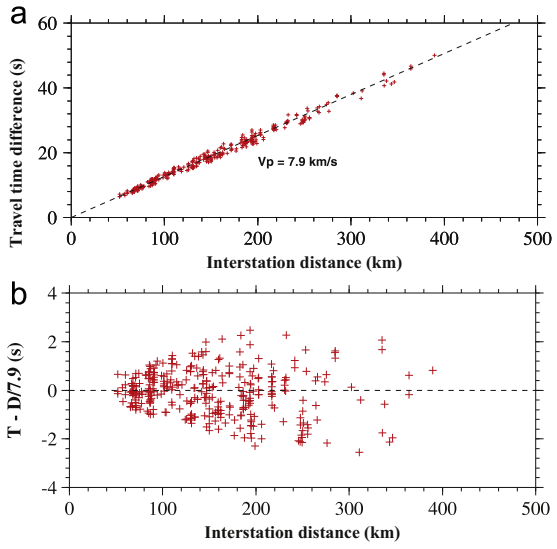

Fig. 5. (a) Average *Pn* velocity of 7.9 km/s in the uppermost mantle as determined by regression of *Pn* traveltime differences (represented by the dashed line) vs inter-station distance. Data with inter-station distance less than 50 km are not included in the inversion. (b) Reduced traveltime differences with an average *Pn* velocity of 7.9 km/s.

trend is quite clear and the slope is equal to the average *Pn* velocity of the uppermost mantle (~7.9 km/s). Fig. 5b shows the reduced traveltime (with reduced velocity of 7.9 km/s) versus epicenter distance difference for *Pn* arrivals. Lateral variations are more easily recognized in these reduced travel times.

The average crustal *P* wave velocity was determined to be around 6.2 km/s from previous results of traveltime tomography (Lei and Zhao, 2009; Wu et al., 2009; Li et al., 2011a) and deep seismic sounding (Wang et al., 2003; Li et al., 2006b). We changed the average crustal *P* wave velocity from 6.0 to 6.4 km/s in several trial inversions, and found that the prominent characteristics of the velocity image in the uppermost mantle remain unchanged. The Moho depth of 50 km represents the average value of this area (Wang et al., 2003; Xu et al., 2007; Wang et al., 2008a; Liu et al., 2009; Zhang et al., 2009), and is chosen in the final inversion. We also test different average Moho depths (from 45 to 55 km) in the inversion, and the pattern of velocity anomalies remains fairly stable except that the average *Pn* velocity changed to some extent (less than 0.05 km/s). The Moho topography is derived from Bouguer gravity (Jiang and Jin, 2005; Xu et al., 2010a; Li et al., 2011a), deep seismic sounding data (Wang et al., 2003) and receiver functions (Xu et al., 2007; Wang et al., 2008a; Liu et al., 2009; Zhang et al., 2009), and is used to correct for the *Pn* traveltimes in the station-side crust during the inversion.

3. Results

3.1. Results of inversion

Residuals of interstation *Pn* wave traveltime differences before and after the inversion are plotted as a function of back azimuth and inter-station distance (Fig. 6a–d). A posteriori residual standard deviations are also reduced from 0.89 s for the starting model to 0.18 and 0.15 s for grid-spacing with $0.5^\circ \times 0.4^\circ$ and $0.25^\circ \times 0.2^\circ$ (Fig. 6e and f) in longitudinal and latitudinal directions, respectively. It suggests that both preferred models fit the observed data very well despite their different grid spacing. As shown in Fig. 6g, most of the back azimuth differences of *Pn* traveltime difference data are less than 3°, which satisfies the requirement of the *Pn* traveltime difference tomography technique (i.e., the *Pn* wave traveltimes on the overlapped ray paths are approximately the same).

The inversion results of *Pn* velocity with two models of $0.5^\circ \times 0.4^\circ$ and $0.25^\circ \times 0.2^\circ$ grid spacing are superimposed upon shaded topography and cover most of the LFB (Fig. 7a and b). Results from the two models are very similar even though different grid spacings are adopted, which shows the robustness of the tomographic inversion. In the following, only the prominent velocity anomalies shown in the two models are discussed.

A high *Pn* velocity of ~8.1 km/s (~2–3% higher than the background velocity of 7.9 km/s) is found beneath the Sichuan Basin, whereas relative low velocity (< 7.8 km/s, ~2% lower than the background) is found beneath the eastern Tibetan plateau and to the southwest of Sichuan Basin. A pronounced feature of the *Pn* velocities are the distinct anomalies beneath the southwestern and northeastern portions of the LFB beginning from ~N31.5°. The southwestern portion of the LFB is parallel to the boundary separating the low and high *Pn* velocities in its two sides. In contrast, the northeastern portion is dominated by relative high *Pn* velocity (~8.0 km/s, ~1% higher than the background) and the boundary between low and high *Pn* velocity anomalies migrates westward tens of kilometers relative to the LFB. Significantly low *Pn* velocity (< 7.8 km/s, ~2% lower than the background) also is shown to the south of the Sichuan Basin. However, this velocity anomaly is far away from the LFB, and is most likely not related to the seismo-tectonics of Wenchuan earthquakes.

3.2. Resolution and error analysis

In order to estimate the resolution of the tomography model, we perform a series of checkerboard resolution tests with different anomaly sizes and grid spacing (Fig. 8). The results indicate that velocity anomalies with $0.5^\circ \times 0.4^\circ$ or smaller sizes can be resolved in most areas with good ray path coverage, especially in the vicinity of the LFB. At the edge of raypath distribution, the pattern cannot be well resolved due to the absence of crossing ray paths.

Compared to the standard *Pn* traveltime tomographic method, the travel time difference method is minimally affected by errors in earthquake mislocation (especially the focal depth) and origin time. Errors from lateral crustal structure will be partially

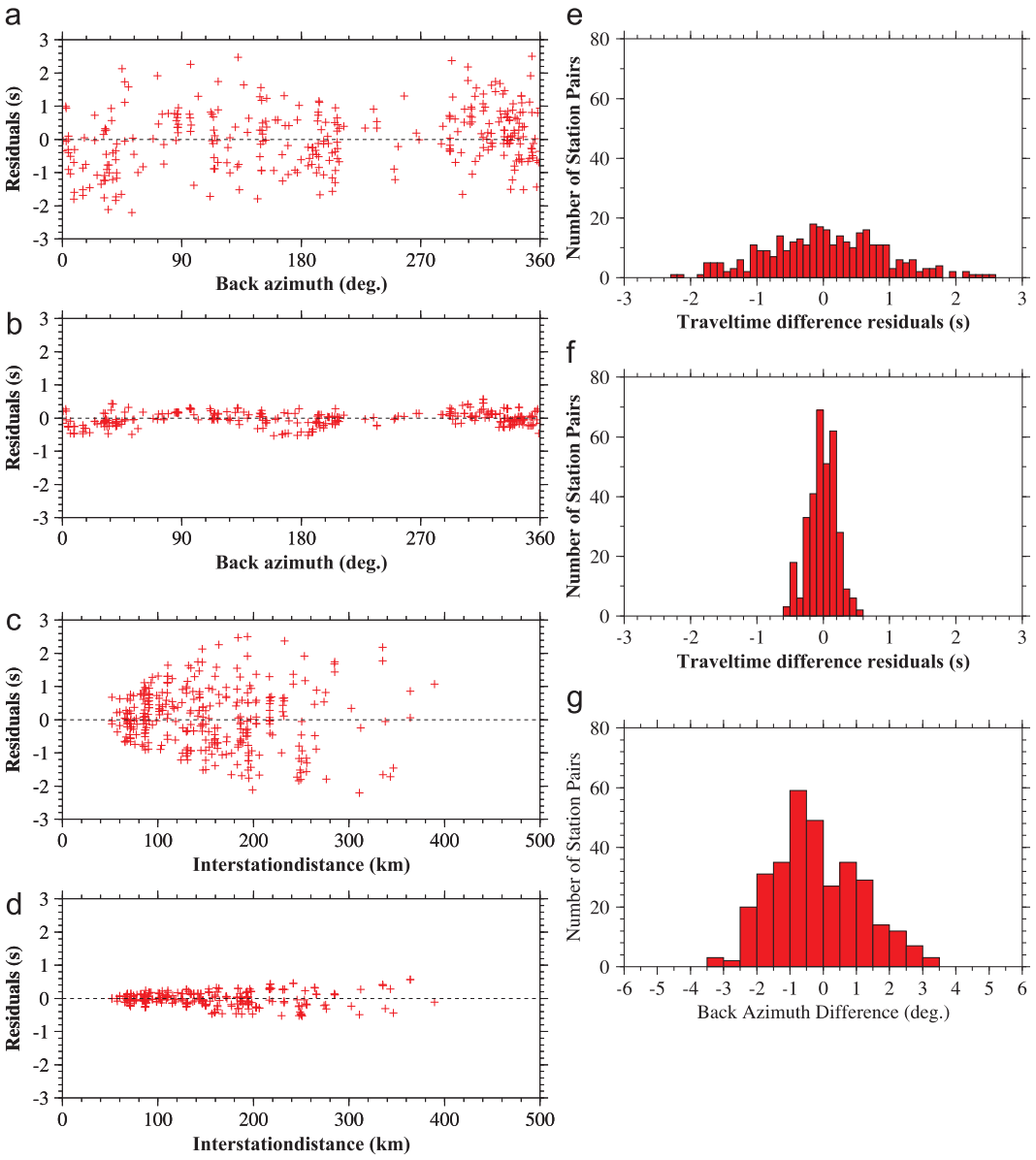

Fig. 6. (a) and (b) show the variations of *Pn* traveltime difference residuals before and after the inversion, respectively, with different back-azimuths of ray paths. (c) and (d) show the variations of *Pn* traveltime difference residuals before and after the inversion with different interstation distance. (e) and (f) are the residual histograms of *Pn* traveltime differences before and after the inversion. (g) The number of station pairs with different back azimuth.

absorbed as part of the station delay. In our result, the station delays vary from −0.10 to 0.29 s, but we did not find apparent correlations with the crustal thickness. One possible reason for small station delays and absence of correlations may be the few arrivals per station (totally 328 *Pn* traveltime differences for 57 stations) (Hearn et al., 2004) and the traveltime difference technique for pairs of stations, which limits the interpretation of station delays. The correction of *Pn* traveltimes with Moho topography will also diminish some effects on the station delay from lateral variations of crustal thickness (Li et al., 2011b).

In order to estimate the effects of Moho topography on the *Pn* velocity imaging and to verify the validity of *Pn* traveltime correction with 3D Moho depth, inversions with synthetic *Pn* traveltime difference data are carried out in the same way as the inversion with real data. The velocities of synthetic model are set to be 6.2 km/s in the crust and 7.9 km/s in the mantle. Moho topography used in previous studies are adopted (Xu et al., 2010a; Li et al., 2011a). Traveltimes for *Pn* arrivals are calculated using an algorithm that adapts the finite difference eikonal equation solver in spherical coordinates (Hole and Zelt, 1995). This approach has been used in several 3-D tomographic studies and proved effective for strongly heterogeneous 3-D velocity model (Roecker et al., 2006, 2010; Li et al., 2009b). In this particular application, a fine grid spacing of ~1 km is chosen for traveltime calculation. Fig. 9a and b shows the restored *Pn* velocity images with $0.5^\circ \times 0.4^\circ$ and $0.25^\circ \times 0.2^\circ$ grid spacing, respectively. The size of the restored velocity anomaly is within 0.1 km/s of the input model, and is much smaller in most areas of study region. Moreover, no apparent correlations are found between the restored *Pn* velocity and the Moho depth, thus arguing against possible artifacts in the tomography model due to 3D Moho depths.

4. Discussion

Our result indicates significant variations in *Pn* wave velocities in the uppermost mantle beneath the eastern Tibetan plateau and the Sichuan Basin. The prominent features of high *Pn* velocities

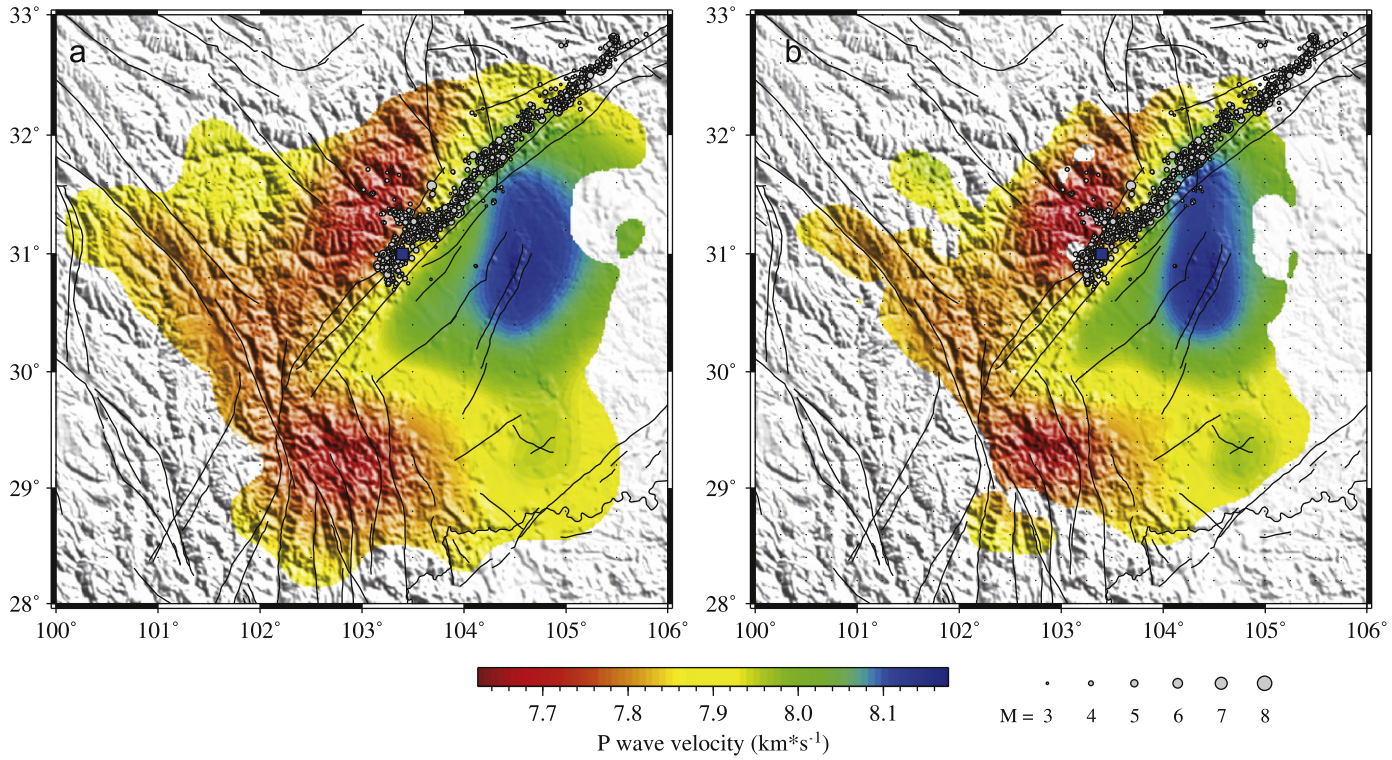

Fig. 7. *Pn* velocities of the uppermost mantle. (a) is the result from an inversion model with $0.5^\circ \times 0.4^\circ$ grid spacing, and (b) with $0.25^\circ \times 0.2^\circ$ spacing. Black lines indicate the fault traces and gray circles indicate aftershocks of the Wenchuan earthquake. Only the velocities with ray path hit counts greater than 2 are plotted.

beneath the Sichuan Basin and low velocities beneath the eastern Tibetan plateau are similar to previous *Pn* tomographic results in this region (Hearn et al., 2004; Liang et al., 2004; Liang and Song, 2006; Pei et al., 2007; Phillips et al., 2005, 2007; Cui and Pei, 2009; Xu and Song, 2010; Xu et al., 2010b), suggesting the robustness of this feature. Moreover, our method minimizes the errors from earthquake mislocation and original time, and more reliable images of detailed *Pn* velocity structures are expected. Previous 3-D traveltime tomography (Huang and Zhao, 2006; Lei and Zhao, 2009; Guo et al., 2009; Wu et al., 2009; Xu and Song, 2010), surface wave tomography with ambient noise (Yao et al., 2008; Li et al., 2009a, 2010a; Yang et al., 2010; Zheng et al., 2010) and density inversion from Bouguer gravity (Lou et al., 2009) reported low *P* and *S* velocities and low density in the lower crust in the eastern Tibetan plateau in contrast to high *P* and *S* velocities and high density in the lower crust in the Sichuan Basin. Joint local and teleseismic traveltime tomography also provide similar velocity anomalies in this area (Li et al., 2006a; Huang and Zhao, 2006; Guo et al., 2009).

Distinct *Pn* velocities imply different characteristics of the mantle lid. The low velocities from lower crust to uppermost mantle beneath the eastern Tibetan plateau may suggest a weak and ductile lithosphere. In contrast, high *Pn* velocities in the Sichuan Basin are consistent with the high velocities in the low crust and upper mantle, suggesting a stable and rigid cratonic lithosphere. The *Pn* velocity anomaly is believed to be sensitive to temperature, fluid content and pressure (McNamara et al., 1997; Hearn et al., 2004). Low *Pn* velocities beneath the eastern Tibetan plateau may partially reflect a very thin lithosphere (70–80 km) (Zhang et al., 2010), implying that hot asthenosphere may increase the temperature and reduce the strength of the lithospheric mantle, thus promoting lower crust flow. The *P* wave velocity images at 90 and 150 km depths from teleseismic arrival time tomography with onsets recorded by 163 temporary seismic stations in this area (Guo et al., 2009) also suggest low velocity anomalies (1–3% lower than the background) in eastern Tibet, and high velocity anomalies (1–3% higher than the background) in the Sichuan Basin. Although the amplitudes of these anomalies are somewhat different from our *Pn* result (*Pn* velocities 2% lower and 2–3% higher than the background) the patterns of velocity anomalies remain similar. Both results suggest that the deeper parts of the upper mantle contain a source of heat that creates the low velocity anomalies (possibly resulting from high temperature) in the uppermost mantle. Deep seismic sounding and receiver functions also indicate that crustal thickness across the LFB shows a step-like increase of about 20 km in the Moho depth (Wang et al., 2003, 2008a; Li et al., 2006b; Zhang et al., 2009). High *Vp*/*Vs* ratio ($\sim$1.80) and low *S* velocity from receiver functions and surface wave tomography with seismic ambient noise imply partial melting in the lower crust beneath the eastern Tibetan plateau (Xu et al., 2007; Wang et al., 2008a; Yao et al., 2008; Liu et al., 2009; Li et al., 2010). Those above results, together with the steep topography gradient along the LFB, suggest that the eastward crustal flow of the eastern Tibetan plateau are probably blocked by the rigid lithosphere of the Sichuan Basin (Royden et al., 1997, 2008; Clark and Royden, 2000; Klemperer, 2006; Burchfiel et al., 2008; Zhang et al., 2009, 2010; Xu et al., 2010a). It could be responsible not only for the collisional shortening, crustal thickening and relief uplifting in the southeastern or northeastern Tibetan plateau around the rigid Sichuan Basin, but also for the occurrence of the Wenchuan earthquake. Long-term uplift driven by lower crust and upper mantle with slow convergence and right-lateral strike slip of the eastern Tibetan plateau accumulated the stress that triggered the Wenchuan earthquake.

Comparing the variations of the *Pn* velocity anomaly with the location and geometry of the LFB, we find that the rapid variations of the anomaly are parallel to the southwestern portion of the LFB. In contrast, the boundary of low and high *Pn* velocity anomalies migrate westward tens of kilometers relative to the

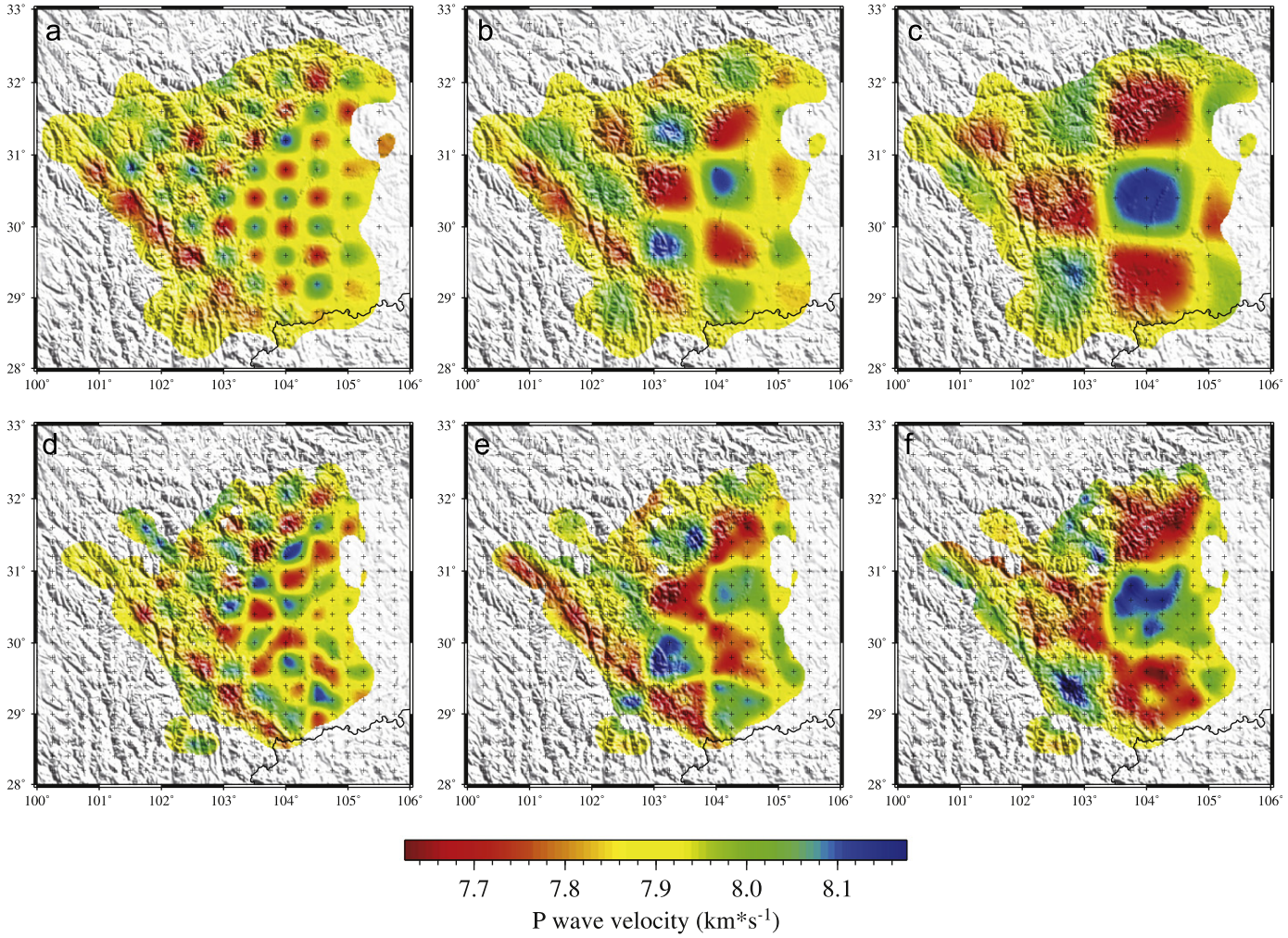

Fig. 8. Checkerboard resolution tests for different anomaly sizes and grid spacing of the models. (a), (b), and (c) are for the test models with inversion grid spacing of $0.5^\circ \times 0.4^\circ$, and (d), (e), and (f) are the test models with inversion node spacing of $0.25^\circ \times 0.2^\circ$. Black crosses in each map show the nodes for the inversion. The anomaly sizes for resolution tests are $0.5^\circ \times 0.4^\circ$ (a and e), $1.0^\circ \times 0.8^\circ$ (b and d), $1.5^\circ \times 1.2^\circ$ (c and f). Only the velocities with ray path hit counts greater than 2 are plotted.

northeastern portion of the LFB. We also found a close correspondence between the distribution of *Pn* velocity and the smoothed topography (Fig. 10). High elevations (~4000 m) in the eastern Tibetan plateau corresponds to low *Pn* velocity, and low elevation (~500 m) in the Sichuan Basin corresponds to the *Pn* velocity. The transition belt between the high and low *Pn* velocities also has a good correlation with the rapid increase of elevation from ~500 to ~4000 m. In particular, the 2500 m elevation contour is approximately coincident with the boundary of the high and low *Pn* velocities, rather than along the entire LFB (Fig. 10). Compared to the crustal thickness derived from receiver functions (Xu et al., 2007; Lou et al., 2009; Wang et al., 2010) and deep seismic sounding (Li et al., 2006b), crustal thickness does not correlate with the northeastern portion of the LFB. On the other hand, crustal thickness, as well as the density variations in the uppermost mantle (Lou et al., 2009), corresponds well to the *Pn* velocity anomalies. Since the crust in the eastern Tibetan plateau is believed to be in Airy-type isostatic equilibrium (Xu et al., 2007; Wang et al., 2010), the consistency of *Pn* velocity anomalies with the crustal thickness, smoothed topography and Bouguer gravity (Jiang and Jin, 2005) is expected, implying that the dynamic processes of the lithosphere mantle are the primary causes for crustal thickening and relief uplift in the eastern Tibetan plateau.

Of particular interest is the different pattern of *Pn* velocity anomalies along southwestern and northeastern portions of the LFB, approximately beginning from ~N31.5°, which is closely related to the distinct characteristics of the two segments of the LFB. The faults separating the LFB into two segments are the Huya and Leidong faults (Chen et al., 2007) (Fig. 1). The southwestern portion of the LFB consists of three faults, i.e., Wenchuan-Maoxian fault, Yingxiu-Beichuan fault and Guanxian-Jiangyou fault (Fig. 1), which coincides approximately with the steep topography gradient and with the boundary between low and high *Pn* velocity. The northeastern portion of the LFB has only one fault trace, the Yingxiu-Beichuan fault. The topography gradient in this area is much smaller (the elevations changes from ~500 to ~1500–2500 m), and a relatively high *Pn* velocity also is present (Fig. 10). The Bouguer gravity data also clearly delineate an anomalous belt along the Huya and Leidong faults the separates the two segments of the LFB, and the trend and gradient of the gravity contours appear to change along the LFB (Chen et al., 2007). In the rupture process of the Wenchuan earthquake, the slip distribution is characterized by two separated regions with slip exceeding 7 m in the southwestern and northeastern portions of the LFB (Ji and Hayes, 2008; Wang et al., 2008b), suggesting two relatively independent ruptures. All three fault traces in the southwestern portion of the LFB completely ruptured the surface, while only

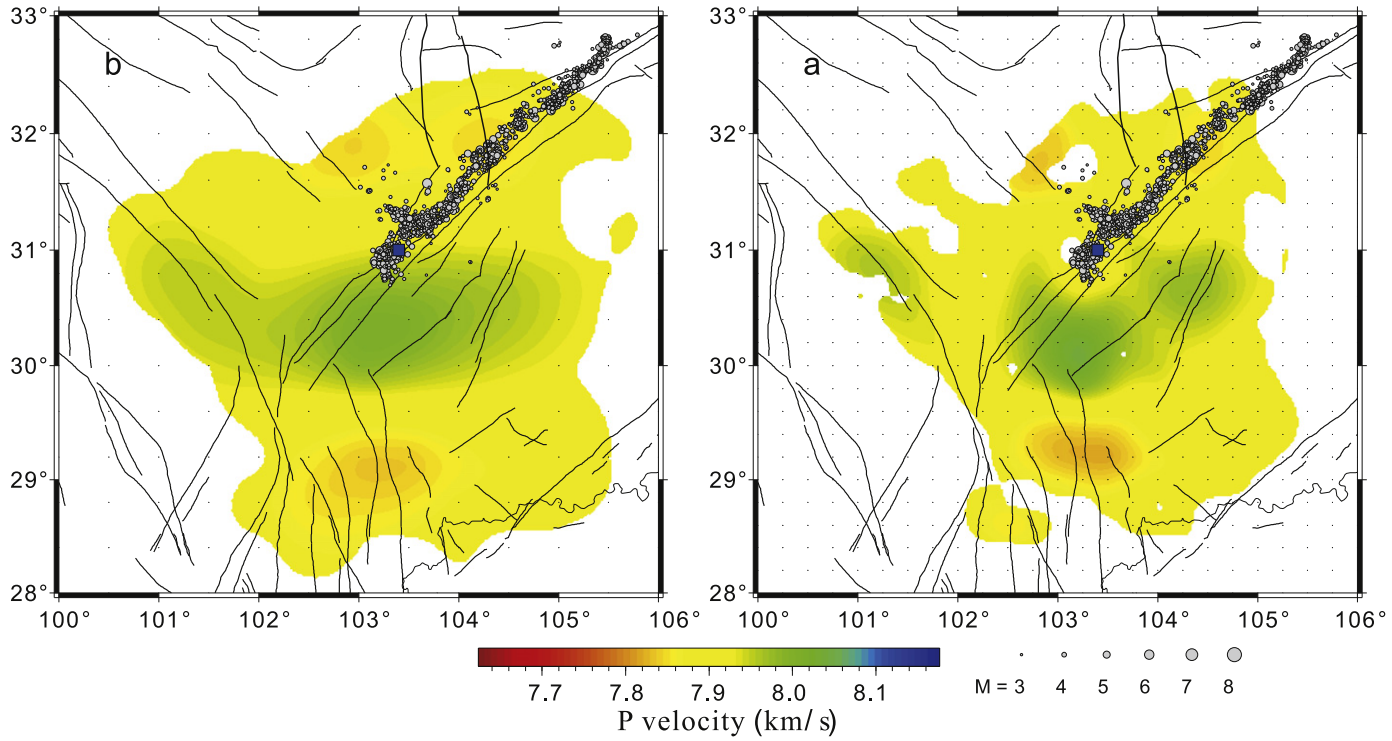

Fig. 9. Recovered *Pn* velocities in the uppermost mantle with synthetic traveltimes from a test model with an undulating Moho. The grid spacing is $0.5^\circ \times 0.4^\circ$ for (a) and $0.25^\circ \times 0.2^\circ$ for (b).

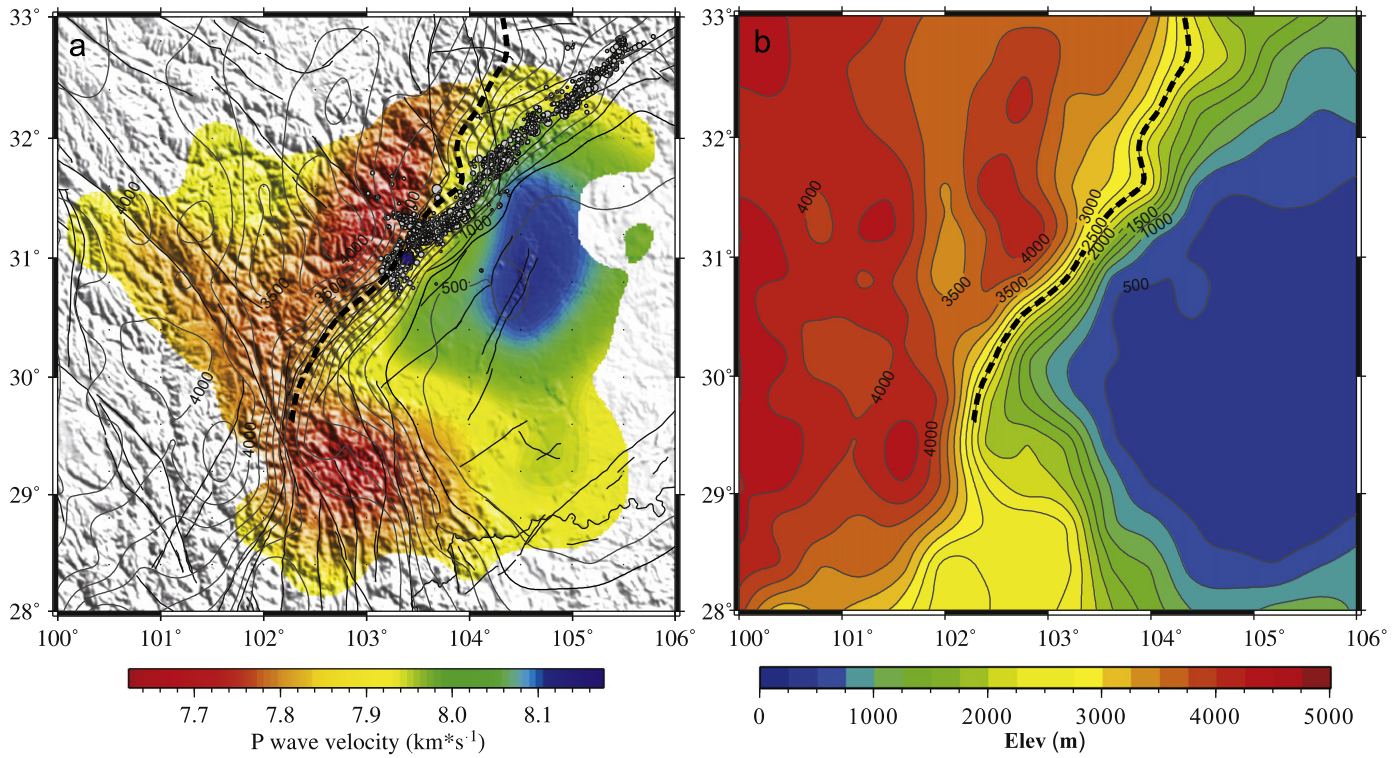

Fig. 10. (a) *Pn* velocities and (b) the smoothed elevations with a $0.4^\circ \times 0.35^\circ$ grid spacing. Note that the black dashed lines in both (a) and (b) represent the contour of 2500 m elevation, which is roughly coincident with the boundary of low and high *Pn* velocities near the Longmenshan Fault Belt. The gray lines represent the elevation contours with 500 m interval. The node spacing for *Pn* velocity model is $0.5^\circ \times 0.4^\circ$. Note that (a) is same as Fig. 7a.

part of the Yingxiu-Beichuan fault in the northeastern portion ruptured the surface. Moreover, in the southwestern portion of the LFB, the rupture is dominated by thrust motion with a dip angle of 30–50°, and the component of strike-slip is relative small. In comparison, the rupture in the northeastern portion is characterized by both thrust and strike-slip with a larger dip angle of 70–90° (Wang et al., 2008b; Xu et al., 2008; Zheng et al., 2009; Luo et al., 2010). The historical seismicity is also very distinct for

the two segments of the LFB. Before the Wenchuan earthquake, only 3 earthquakes with magnitude of 6–6.5 occurred since the year of 1657 in the southwestern portion, while no strong earthquakes were found in the northeastern portion (Wen, 1995; Chen et al., 2007).

The significant contrast in *Pn* velocity anomalies, topography gradient, rupture process, and historical seismicity between the southwestern and northeastern portions of the LFB may reflect the relative importance of the crust and lithospheric mantle in local tectonics. The aftershocks of Wenchuan earthquake are confined to depths of less than 30 km along the LFB (Huang et al., 2008; Chen et al., 2009; Zheng et al., 2009; Luo et al., 2010), suggesting that only the upper crust is involved in the co-seismic process. Therefore, the mismatch between geographic pattern of *Pn* and seismic features of the LFB argues against simplistic models that the geodynamic processes in the uppermost mantle impose direct control over faults in the upper crust. Instead, seismic behavior of faults may be controlled by a balance between gravitational potential energy (buoyancy) and tectonic forces (Jones et al., 1996; England and Molnar, 1997). For example, the topographic gradient at the southwestern portion of LFB is the steepest in the world, where gravity may play a dominant role. The topographic gradient is much less at the northeastern portion of LFB, and the fault could be controlled by both gravity and far field tectonic stresses. Moreover, different lithologies across the LFB may also play a role in the segmentation. The southern portion of LFB features a hanging wall of Proterozoic basement rocks, while the northern portion contains a hanging wall of Cambrian-Ordovician rocks (Jia et al., 2010).

5. Conclusions

We constructed an image of the *Pn* wave velocity in the uppermost mantle beneath the eastern margin of the Tibetan plateau with interstation *Pn* traveltime difference data. Our image beneath the eastern margin of the Tibetan plateau is consistent with those determined in previous studies with standard *Pn* tomography method and other seismological methods. However, our method can minimize the errors from earthquake mislocation and original time, and achieve a more reliable image of detailed *Pn* velocity structure. Our results confirm that in the uppermost mantle, there are significant low *Pn* velocities beneath the eastern Tibetan plateau and high *Pn* velocities beneath the Sichuan Basin, which is consistent with the interpretation that the rigid and stable lithosphere of the Sichuan Basin may act as a barrier to the eastward escape flow of the ductile crust and lithosphere of the eastern Tibetan plateau (Zhang et al., 2010). The *Pn* velocities are in good correspondence to the smoothed topography, crustal thickness and Bouguer gravity, suggesting that the dynamic processes of the lithosphere mantle should be responsible for the crustal thickening and relief in the eastern Tibetan plateau. The distinct characteristics of the two segments of the LFB, such as significant changes in topography gradient, historical seismicity, coseismic rupture features and aftershock distribution of Wenchuan earthquake, suggest different tectonic roles of the crust and lithospheric mantle. Based on the inconsistency of aftershock distribution (focal depth < 30 km), topographic gradient and the variations in *Pn* velocities across the southwestern and northeastern segments of the LFB, we propose that gravity and tectonic forces may be the cause of the segmentation of LFB. However, we only studied the *Pn* velocities of the uppermost mantle, which provide only limited information on geodynamical processes. More geophysical studies (such as anisotropy, *Sn* velocity, attenuation, etc.) are required to understand the reason for the segmentation.

Acknowledgments

We thank Prof. Shearer P. M., Prof. Phillips S. and an anonymous reviewer for their detailed comments that improve the manuscript. We are grateful to the Sichuan Earthquake Network for providing seismic arrival time data. We benefited from discussions with Youshun Sun, Shunping Pei, Jiuhui Chen, Lianfeng Zhao and Yong Zheng. This work was supported by NSFC (41074032),CAS fund and special fund from the State Key Laboratory of Geodesy and Earth's Dynamics.

References

Burchfiel, B.C., Royden, L.H., van der Hilst, R.D., et al., 2008. A geological and geophysical context for the Wenchuan earthquake of 12 May 2008, Sichuan, People's Republic of China. GSA Today 18, 4–11.

Chen, G.G., Ji, F.J., Zhou, R.J., et al., 2007. Primary research of activity segmentation of Longmenshan Fault Zone since Late-Quaternary. Seismol. Geol. 29 (3), 657–673.

Chen, J.H., Liu, Q.Y., Li, S.C., et al., 2009. Seismotectonic study by relocation of the Wenchuan Ms 8.0 earthquake sequence. Chin. J. Geophys. 52 (2), 390–397.

Clark, M.K., Royden, L.H., 2000. Topographic ooze: building the eastern margin of Tibet by lower crustal flow. Geology 28 (8), 703–706.

Cui, Z.X., Pei, S.P., 2009. Study on Pn velocity and anisotropy in the uppermost mantle of the Eastern Himalayan Syntaxis and surrounding regions. Chin. J. Geophys. 52 (9), 2245–2254.

England, P.C., Molnar, P., 1997. Active deformation of Asia: from kinematics to dynamics. Science 278, 647–650.

Guo, B., Liu, Q., Chen, J., et al., 2009. Teleseismic P-wave tomography of the crust and upper mantle in Longmen Shan area, west Sichuan. Chin. J. Geophys. 52 (2), 346–355.

Hearn, T.M., 1996. Anisotropic Pn tomography in the western United States. J. Geophys. Res. 101, 8403–8414.

Hearn, T.M., Wang, S., Ni, J.F., et al., 2004. Uppermost mantle velocities beneath China and surrounding regions. J. Geophys. Res. 109, B11301.

Hole, J.A., Zelt, B.C., 1995. 3-D finite-difference reflection traveltimes. Geophys. J. Int. 121, 427–434.

Huang, J., Zhao, D., 2006. High-resolution mantle tomography of China and surrounding regions. J. Geophys. Res. 111, B09305.

Huang, Y., Wu, J.P., Zhang, T.Z., et al., 2008. Relocation of the M8.0 Wenchuan earthquake and its aftershock sequence. Sci. China Ser. D-Earth Sci. 51 (12), 1703–1711.

Ji, C., Hayes, G., 2008. Finite fault model: preliminary result of the May 12, 2008 Mw 7.9 eastern Sichuan China earthquake, . 〈http://earthquake.usgs.gov/earthquakes/eqinthenews/2008/us2008ryan/finite_fault.php〉.

Jia, D., Li, Y., Lin, A., et al., 2010. Structural model of 2008 M_w 7.9 Wenchuan earthquake in the rejuvenated Longmen Shan thrust belt, China. Tectonophysics 491, 174–184.

Jiang, X., Jin, Y., 2005. Mapping the deep lithospheric structure beneath the eastern margin of the Tibetan Plateau from gravity anomalies. J. Geophys. Res. 110, B07407.

Jones, C.H., Unruh, J.R., Sonder, L.J., 1996. The role of gravitational potential energy in the active deformation of the southwestern United States. Nature 381, 37–41.

Klemperer, S.L., 2006. Crustal flow in Tibet: a review of geophysical evidence for the physical state of Tibetan lithosphere. In: Searle, M.P., Law, R.D. (Eds.), Channel Flow, Ductile Extrusion and Exhumation of Lower Mid-crust in Continental Collision Zones, Geol. Soc. Spec. Pub., 268, pp. 39–70.

Lei, J.S., Zhao, D.P., 2009. Structural heterogeneity of the Longmenshan fault zone and the mechanism of the 2008 Wenchuan earthquake (M_s 8.0). Geochem. Geophys. Geosyst. 10, 10.

Li, C., van der Hislt, R.D., Toksoz, M.N., 2006a. Constraining spatial variations in the upper mantle beneath SE Asia. Phys. Earth Planet. Int. 154, 180–195.

Li, H., Su, W., Wang, C., et al., 2009a. Ambient noise Rayleigh wave tomography in western Sichuan and eastern Tibet. Earth Planet. Sci. Lett. 282, 201–211.

Li, S., Mooney, W.D., Fan, J., 2006b. Crustal structure of mainland China from deep seismic sounding data. Tectonophysics 420, 239–252.

Li, Y., Yao, H.J., Liu, Q.Y., 2010. Phase velocity array tomography of Rayleigh waves in western Sichuan from ambient seismic noise. Chin. J. Geophys. 53 (4), 842–852.

Li, Z.W., Roecker, S., Li, Z.H., et al., 2009b. Tomographic image of the crust and upper mantle beneath the western Tien Shan from the MANAS broadband deployment: possible evidence for lithospheric delamination. Tectonophysics 477, 49–57.

Li, Z.W., Xu, Y., Huang, R., et al., 2011a. Crustal P-wave velocity structure of the Longmen Shan region and its tectonic implications for the 2008 Wenchuan earthquake. Sci. China Earth Sci. 54, 1386–1393.

Li, Z.W., Hao, T.Y., Xu, Y., 2011b. Uppermost mantle structure of the North China Craton: constraints from interstation Pn traveltime difference tomography. Chin. Sci. Bull. 56, 1691–1699.

Liang, C., Song, X., Huang, J., 2004. Tomographic inversion of Pn traveltimes in China. J. Geophys. Res. 109, B11304.
Liang, C., Song, X., 2006. A low velocity belt beneath northern and eastern Tibetan Plateau from Pn tomography. Geophys. Res. Lett. 33, L22306.
Liu, Q.Y., Li, Y., Chen, J.H., et al., 2009. Wenchuan *Ms* 8.0 earthquake: preliminary study of the S-wave velocity structure of the crust and upper mantle. Chin. J. Geophys. 52 (2), 309–319.
Lou, H., Wang, C.Y., Lv, Z.Y., et al., 2009. Deep tectonic setting of the 2008 Wenchuan *Ms*8.0 earthquake in southwestern China—Joint analysis of teleseismic P-wave receiver functions and Bouguer gravity anomalies. Sci. China Ser. D—Earth Sci. 52, 166–179.
Luo, Y., Ni, S.D., Zeng, X.F., et al., 2010. A shallow aftershock sequence in the northeastern end of the Wenchuan earthquake aftershock zone. Sci. China Earth Sci. 53, 1655–1664.
McNamara, D.E., Walter, W.R., Owens, T.J., et al., 1997. Upper mantle velocity structure beneath the Tibetan Plateau from Pn traveltime tomography. J. Geophys. Res. 102 (B1), 493–505.
Molnar, P., Tapponnier, P., 1975. Cenozoic tectonics of Asia: effects of a continental collision. Science 189, 419–426.
Molnar, P., 1988. A review of geophysical constraints on the deep structure of the Tibetan Plateau, the Himalaya and the Karakoram, and their tectonic implications. Trans. R. Soc. London Ser. A 327, 33–88.
Paige, C.C., Saunders, M.A., 1982. LSQR: an algorithm for sparse linear equations and sparse least squares. TOMS 8 (1), 43–71.
Pei, S., Zhao, J., Sun, Y., et al., 2007. Upper mantle seismic velocities and anisotropy in China determined through Pn and Sn tomography. J. Geophys. Res. 112, B05312.
Phillips, W.S., Rowe, C.A., Steck, L.K., 2005. The use of interstation P wave arrival time differences to account for regional path variability. Geophys. Res. Lett. 32, L11301.
Phillips, W.S., Begnaud, M.L., Rowe, C.A., et al., 2007. Accounting for lateral variations of the upper mantle gradient in Pn tomography studies. Geophys. Res. Lett. 34, L14312.
Roecker, S., Thurber, C., Roberts, K., et al., 2006. Refining the image of the San Andreas Fault near Parkfield, California using a finite difference traveltime computation technique. Tectonophysics 426, 189–205.
Roecker, S., Baker, B., McLaughlin, J., 2010. A finite-difference algorithm for full waveform teleseismic tomography. Geophys. J. Int. 181 (2), 1017–1040.
Royden, L.H., Burchfiel, B.C., King, R.W., et al., 1997. Surface deformation and lower crustal flow in eastern Tibet. Science 276, 788–790.
Royden, L.H., Burchfiel, B.C., van der Hilst, R.D., 2008. The geological evolution of the Tibetan plateau. Science 321, 1054–1058.
Seward, A.M., Henderson, C.M., Smith, E.G.C., 2009. Models of the upper mantle beneath the central North Island, New Zealand, from speeds and anisotropy of subhorizontal P waves (Pn). J. Geophys. Res. 114, B01301.
Sun, Y., Kuleli, S., Morgan, D.F., et al., 2004. Location robustness of earthquakes in Sichuan Province, China. Seismol. Res. Lett. 75 (1), 54–62.
Waldhauser, F., Ellsworth, W.L., 2000. A double-difference earthquake location algorithm: method and application to the northern Hayward Fault. California Bull. Seismol. Soc. Am. 90, 1353–1368.
Wang, C.Y., Wu, J.P., Lou, H., et al., 2003. P-wave crustal velocity structure in western Sichuan and eastern Tibetan region. Sci. China—Ser. D Earth Sci. 33 (Suppl.), 181–189.
Wang, C.Y., Lou, H., Lu, Z., et al., 2008a. S-wave crustal and upper mantle's velocity structure in the eastern Tibetan Plateau—deep environment of lower crustal flow. Sci. China Ser. D.—Earth Sci. 51, 263–274.
Wang, W.M., Zhao, L.F., Li, J., et al., 2008b. Rupture process of the Ms 8.0 Wenchuan earthquake of Sichuan. Chin. J. Geophys. 51 (5), 1403–1410.
Wang, C.Y., Lou, H., Silver, P.G., et al., 2010. Crustal structure variation along 30°N in the eastern Tibetan Plateau and its tectonic implications. Earth Planet. Sci. Lett. 289, 367–376.
Wen, X.Z., 1995. Quantitative Assessments of Earthquake Potential on Active Faults. Seismological Press, Beijing.
Wu, J.P., Huang, Y., Zhang, T.Z., et al., 2009. Aftershock distribution of the Ms 8.0 Wenchuan earthquake and three dimensional P-wave velocity structure in and around source region. Chin. J. Geophys. 52 (2), 320–328.
Xu, L., Rondenay, S., van der Hilst, R.D., 2007. Structure of the crust beneath the southeastern Tibetan Plateau from teleseismic receiver functions. Phys. Earth Planet. Int. 165, 176–193.
Xu, X.W., Wen, X.Z., Ye, J.Q., et al., 2008. The Ms 8.0 Wenchuan earthquake surface ruptures and its seismogenic structure. Seismol. Geol. 30 (3), 597–629.
Xu, Z., Song, X., 2010. Joint inversion for crustal and Pn velocities and Moho depth in Eastern margin of the Tibetan Plateau. Tectonophysics 491, 185–193.
Xu, Y., Li, Z., Huang, R., et al., 2010a. Seismic structure of the Longmen Shan region from S-wave tomography and its relationship with the Wenchuan Ms 8.0 earthquake on 12 May 2008, sourthwestern China. Geophys. Res. Lett. 37, L02304.
Xu, Y., Li, Z., Huang, R., et al., 2010b. Pn-wave velocity and anisotropy of the western Sichuan and Longmen Mountain region, China. Sci. China Earth Sci. 53, 1665–1670.
Yao, H., Beghein, C., van der Hilst, R.D., 2008. Surface-wave array tomography in SE Tibet from ambient seismic noise and two-station analysis: II. Crustal and upper mantle structure. Geophys. J. Int. 173, 205–219.
Yang, Y., Zheng, Y., Chen, J., et al., 2010. Rayleigh wave phase velocity maps of Tibet and the surrounding regions from ambient seismic noise tomography. Geochem. Geophys. Geosyst. 11, Q08010.
Zhang, H., Thurber, C.H., 2003. Double-difference tomography: the method and its application to Hayward Fault. California Bull. Seismol. Soc. Am. 93, 1875–1889.
Zhao, L., Xie, J., 1993. Lateral variations in compressional velocities beneath the Tibetan plateau from Pn travel-time tomography. Geophys. J. Int. 115, 1070–1084.
Zhang, P.Z., Shen, Z., Wang, M., et al., 2004. Continuous deformation of the Tibetan plateau from global positioning system data. Geology 32, 809–812.
Zhang, P.Z., Xu, X.W., Wen, X.Z., et al., 2008. Slip rates and recurrence intervals of the Longmen Shan active fault zone, and tectonic implications for the mechanism of the May 12 Wenchuan earthquake, 2008, Sichuan, China. Chin. J. Geophys. 51 (4), 1066–1073.
Zhang, Z., Wang, Y., Chen, Y., et al., 2009. Crustal structure across Longmenshan fault belt from passive source seismic profiling. Geophys. Res. Lett. 36, L17310.
Zhang, Z.J., Yuan, X.H., Chen, Y., et al., 2010. Seismic signature of the collision between the east Tibetan escape flow and the Sichuan Basin. Earth Planet. Sci. Lett. 2010 (292), 254–264.
Zheng, Y., Ma, H., Lu, Y., et al., 2009. Source mechanism of strong aftershocks ($Ms \geq 5.6$) of the 2008/05/12 Wenchuan earthquake and the implication for seismotectonics. Sci. China Ser. D—Earth Sci. 52, 739–753.
Zheng, Y., Yang, Y.J., Ritzwoller, M.H., et al., 2010. Crustal structure of the northeastern Tibetan plateau, the Ordos block and the Sichuan Basin from ambient noise tomography. Earthq. Sci. 23, 465–476.